Aerospace Science and Technology 124 (2022) 107570

Contents lists available at ScienceDirect

Aerospace Science and Technology

www.elsevier.com/locate/aescte

Multi-UAV cluster-based cooperative navigation with fault detection and exclusion capability

Jiawen Shen [a,b], Shizhuang Wang [a], Xingqun Zhan [a,*]

[a] School of Aeronautics and Astronautics, Shanghai Jiao Tong University, Shanghai, 200240, China
[b] Laboratory of Science and Technology on Marine Navigation and Control, China State Shipbuilding Corporation, China

ARTICLE INFO

Article history:
Received 7 November 2021
Received in revised form 10 March 2022
Accepted 15 April 2022
Available online 21 April 2022
Communicated by Chaoyong Li

Keywords:
Cooperative navigation
Multi-UAV
Clustering
Fault detection and exclusion
Least-squares

ABSTRACT

As a strategy for multiple Unmanned Aerial Vehicle (UAV) systems to commit tasks in complex application environments, cooperative navigation has attracted extensive research interest in recent years. With the increase of the formation scale, centralized cooperative navigation with fully-connected sensors would be inefficient and unreliable. To reduce the computation and communication load, this paper divides the whole system into several groups and designs two categories of cluster-based fusion architectures: locally-centralized structure and distributed structure. The UAV positions are estimated by the least-squares method. Considering the fault modes in multi-UAV systems, a fault detection and exclusion scheme is developed for improving the reliability of the cluster-based cooperative navigation system. MATLAB simulation and Spirent simulator test are carried out to validate the proposed algorithm. To simulate complex environments, the industry-recognized Spirent simulator and Spirent Sim3D software are adopted. The proposed scheme can be applied to both open areas and challenging environments, which has a wide range of applications.

1. Introduction

Multiple Unmanned Aerial Vehicle (UAV) systems have recently attracted increasing attention due to their immense values in both civil and military applications, including UAV-based aerial surveillance, environment monitoring, commercial shows, and small packet delivery [1–3]. Compared with a single UAV, multi-UAV systems can offer significant benefits in inspection scope, error tolerance, and task completion time [4].

As known, high-precision positioning can be achieved by Global Navigation Satellite System (GNSS) in open-sky areas [5]. In urban areas, however, the performance of navigation will be severely degraded due to the poor satellite visibility, heavy multipath interferences and Non-Line-of-Sight (NLOS) receptions, which are caused by signal blockages and signal reflections [6–8]. Such situations may raise great challenges for the navigation of multi-UAV systems. To overcome the aforementioned problems, cooperative navigation have been developed by utilizing information communication from multiple UAVs and increasing the information redundancy [9,10]. Compared with GNSS-only navigation, cooperative navigation fuses ranging information not only from satellites but also from UAVs, which helps enhance availability, robustness and accuracy [11–13]. Nevertheless, cooperative navigation system might face challenges of high network traffic, large calculation amount, and error propagation from the faults occurring on one single UAV to the whole system.

In terms of network traffic and calculation amount, different fusion structures have been developed to improve efficiency. In general, all tasks that demand any type of parameter estimation from multiple sources can benefit from the use of information fusion methods [14]. Based on the type of architecture, fusion structures can be classified into (a) centralized, (b) decentralized, or (c) distributed. The multi-UAV cooperative navigation mainly adopts centralized and distributed structure. In the centralized framework, information from all sensors of each UAV is sent to a unified fusion center for cooperative positioning [15,16]. The centralized structure theoretically provides optimal navigation performance, but it may suffer from heavy communication cost and computational burden when the formation size is large [17]. In a distributed architecture, the UAV can use the received position and ranging information from the adjacent UAVs to fuse with its own sensor data and update its position information [18–20]. Compared with the centralized structure, the distributed one can effectively lower the communication and computational burden. However, it provides suboptimal solutions in terms of accuracy and may face convergence issues caused by poor initial positions [20].

* Corresponding author.
E-mail address: xqzhan@sjtu.edu.cn (X. Zhan).

https://doi.org/10.1016/j.ast.2022.107570
1270-9638/

To further achieve the balance between accuracy and efficiency, cluster-based network has been developed for cooperative localization in Wireless Sensor Network (WSN) [21,22], which can also be referred in cooperative navigation. Tseng proposed a cluster-based cooperative localization to solve the scalability issue of centralized architecture and the initial position issue of distributed architecture by combining the intra-cluster structure with the inter-cluster measurements [23]. Whereas these researches are focused on the cooperative localization problem in WSN with several anchors fixed at known positions [24]. In contrast, there is no known anchors in cooperative navigation for multi-UAV system, which is more complicated.

As for the reliability of the multi-UAV cooperative systems, some Fault Detection and Exclusion (FDE) algorithms have been developed for GNSS-based navigation. Receiver Autonomous Integrity Monitoring (RAIM) [25] and Advanced RAIM (ARAIM) [26] are two representative schemes. However, these two schemes cannot be adapted directly to cooperative navigation since they only use the information of a standalone receiver. Zhuang et al. proposed a Whole-Network Extend Kalman Filter (WNEKF) and an integrity monitoring algorithm based on solution separation strategy and fully-centralized structure, which can monitor all the faults of the whole network simultaneously [11]. Although only few master nodes are required to conduct the algorithm due to the centralized structure, the computation burden and communication load will be heavy. Xiong et al. proposed a cooperative integrity monitoring based on residual decomposition method, which can exploit the GNSS data and inter-vehicle measurements data to detect all the faulty measurements [27]. However, this research adopted a decentralized structure, which may suffer from communication cost problem. Hence, there still exists a research gap in FDE scheme for cluster-based Cooperative Navigation.

In this paper, we aim at two issues in cooperative navigation of multi-UAV system: (a) the balance between efficiency and accuracy of the navigation performance, and (b) the reliability of the navigation solution in fault scenarios. In response, this study considers two categories of cluster-based fusion architectures, i.e., the locally-centralized structure and the distributed structure, and proposes an FDE scheme for cluster-based cooperative navigation. This paper helps validate that the combination of cluster-based cooperative navigation and FDE is feasible and effective. Since the states of the UAVs are estimated by least-squares method, it can be regarded as snapshot navigation which only returns the position when requested [28,29]. The FDE scheme is designed based on solution separation method [26].

The rest of paper is organized as follows. Section 2 describes the measurement models. Section 3 illustrates the multi-UAV cooperative navigation with different fusion structures. Section 4 introduces some fault modes in multi-UAV cooperative navigation and proposes an FDE scheme. Then, simulations are carried out in Section 5 based on MATLAB platform and Spirent Simulator. Finally, Section 6 draws the conclusions and presents some perspectives for future work.

2. Measurement models

This section describes the measurement models in the cooperative navigation system, including the GNSS pseudorange models, the relative ranging measurements and the relative position measurements.

2.1. GNSS pseudorange

Although stable carriers can provide higher accuracy than pseudoranges, they require high-end receivers or favorable signal quality, which are not available in urban areas. Consequently, unsmoothed pseudoranges (i.e., the raw observations provided by receivers) are usually used in GNSS-challenging environments.

For a given receiver on UAV i and a specific satellite s, the pseudorange observation is defined as [30,31]:

$$\rho_i^s = d_i^s + E_i^s + c\left(\delta t_i - \delta t^s\right) + I_i^s + T_i^s + \varepsilon_i^s \tag{1}$$

where the subscript i denotes the individual UAV i and the superscript s denotes the individual satellite; d is the geometrical range between the UAV and the satellite; E is the ephemeris error; c is the speed of light; δt_i denotes the receiver clock offset of UAV i; δt^s denotes the clock offset of satellite s; I represents the ionosphere propagation delay; T represents the troposphere propagation delay; and ε is the pseudorange noise term caused by multipath and receiver noise.

2.2. Peer-to-Peer ranging model

One-dimensional relative range measurement between two vehicles can be obtained directly by ranging modules such as Ultra-Wideband (UWB). The Peer-to-Peer (P2P) ranging measurement is modeled as [13]:

$$m_{ij} = \|\boldsymbol{pos}_j - \boldsymbol{pos}_i\| + \omega_{ij} \tag{2}$$

where m_{ij} is the P2P ranging measurement between UAV i and UAV j; $\boldsymbol{pos}_i$ and $\boldsymbol{pos}_j$ denote the positions of these two UAVs in the local East, North and Up (ENU) coordinate system; $\|\cdot\|$ denotes the L2 norm of relative position vector, i.e., the geometrical range between the two UAVs; and ω is the noise term, which can be modeled as a zero-mean Gaussian distribution with standard deviation of σ_{uwb}.

2.3. Relative position measurement

Generally, relative position measurement can be obtained by visual sensors in or Differential GNSS (DGNSS) and can be expressed in the body axes or the local ENU coordinate system. In this paper, we assume that the three-dimensional relative position measurement is given in local ENU frame, which can be modeled as:

$$\boldsymbol{r}_{ij} = (\boldsymbol{pos}_j - \boldsymbol{pos}_i) + \boldsymbol{v}_{ij} \tag{3}$$

where $\boldsymbol{r}_{ij}$ is the relative position measurement from UAV i to UAV j; and $\boldsymbol{v}$ is the noise vector, which can be modeled as a zero-mean Gaussian distribution with standard deviation of $\boldsymbol{\sigma}_{\text{RP}}$ in three directions.

3. Multi-UAV cooperative navigation with different fusion structures

This section presents three different fusion structures for multi-UAV Cooperative Navigation (CN): the fully-centralized structure for the whole system, the locally-centralized structure for clusters and the distributed structure based on the locally-centralized estimates. The solutions are estimated through least-square method. Section 3.3 analyzes the comparison among these three structures.

3.1. Least squares based centralized CN

The state vector of UAV i is defined as:

$$\boldsymbol{x}_i = \left[x_i^{\text{E}}, x_i^{\text{N}}, x_i^{\text{U}}, \delta \boldsymbol{t}_i\right]^{\text{T}} \tag{4}$$

where the subscript corresponds to the individual UAV; the superscripts E, N, U correspond to the three directions in the local ENU coordinate system. $\delta \boldsymbol{t}_i = [\delta t_{i,\text{G}}, \delta t_{i,\text{R}}, \delta t_{i,\text{C}}, \delta t_{i,\text{E}}]$ denotes the

receiver clock offset corresponding to the satellite system, i.e., GPS, GLONASS, BDS and Galileo.

The absolute observation vector of UAV i is given by:

$$\boldsymbol{z}_i = \boldsymbol{h}_i(\boldsymbol{x}_i) + \boldsymbol{v}_i \tag{5}$$

where $\boldsymbol{z}_i$ is the pseudorange observation vector of UAV i, i.e., $\boldsymbol{z}_i = [\rho_i^1, \rho_i^2, \cdots, \rho_i^{N_i}]^{\mathrm{T}}$, $\boldsymbol{v}_i$ is the measurement noise error, and $\boldsymbol{h}_i$ denotes the observation function corresponding to $\boldsymbol{x}_i$, N_i is the number of the visible satellites to the receiver on UAV i.

The relative observation equation between UAV i and UAV j can be written as:

$$\boldsymbol{z}_{ij} = \boldsymbol{h}_{ij}(\boldsymbol{x}_i, \boldsymbol{x}_j) + \boldsymbol{v}_{ij} \tag{6}$$

where $\boldsymbol{z}_{ij}$ is the relative observation from UAV i to UAV j, i.e., m_{ij} or $\boldsymbol{r}_{ij}$, $\boldsymbol{v}_{ij}$ is the measurement noise error, and $\boldsymbol{h}_{ij}$ denotes the relative observation function of $\boldsymbol{x}_i$ and $\boldsymbol{x}_j$. In this paper, a relative measurement is assumed to be available to both UAVs. Note that, $\boldsymbol{z}_{ij}$ can be replaced by z_{ij} for P2P ranging measurements.

To combine the absolute measurements with the relative observations with n UAVs, the combination and extension of (5) and (6) can be expressed as follows:

$$\begin{bmatrix} \boldsymbol{z}_1 \\ \vdots \\ \boldsymbol{z}_n \\ \boldsymbol{z}_{12} \\ \vdots \\ \boldsymbol{z}_{(n-1)n} \end{bmatrix} = \begin{bmatrix} \boldsymbol{h}_1(\boldsymbol{x}_1) \\ \vdots \\ \boldsymbol{h}_n(\boldsymbol{x}_n) \\ \boldsymbol{h}_{12}(\boldsymbol{x}_1, \boldsymbol{x}_2) \\ \vdots \\ \boldsymbol{h}_{(n-1)n}(\boldsymbol{x}_{n-1}, \boldsymbol{x}_n) \end{bmatrix} + \begin{bmatrix} \boldsymbol{v}_1 \\ \vdots \\ \boldsymbol{v}_n \\ \boldsymbol{v}_{12} \\ \vdots \\ \boldsymbol{v}_{(n-1)n} \end{bmatrix} \tag{7}$$

Equation (7) can be rewritten in a compact form as follows:

$$\boldsymbol{Z} = \boldsymbol{h}(\boldsymbol{X}) + \boldsymbol{V} \tag{8}$$

where $\boldsymbol{X}$ is the state vector of the system, i.e., $\boldsymbol{X} = [\boldsymbol{x}_1^{\mathrm{T}}, \boldsymbol{x}_2^{\mathrm{T}}, \ldots, \boldsymbol{x}_n^{\mathrm{T}}]^{\mathrm{T}}$, and $\boldsymbol{h}$ is a group of nonlinear observation functions, i.e., $\boldsymbol{h} = [\boldsymbol{h}_1, \ldots, \boldsymbol{h}_n, \boldsymbol{h}_{12}, \ldots, \boldsymbol{h}_{(n-1)n}]^{\mathrm{T}}$.

By linearizing $\boldsymbol{h}$ at the estimated state vector $\hat{\boldsymbol{X}} = [\hat{\boldsymbol{x}}_1^{\mathrm{T}}, \hat{\boldsymbol{x}}_2^{\mathrm{T}}, \ldots, \hat{\boldsymbol{x}}_n^{\mathrm{T}}]^{\mathrm{T}}$, (8) can be formed as:

$$\boldsymbol{Z} = \boldsymbol{H}\boldsymbol{X} + \boldsymbol{V} \tag{9}$$

The linearized observation matrix $\boldsymbol{H}$ is defined as [32]:

$$\boldsymbol{H} = \begin{bmatrix} \boldsymbol{H}_1 & \boldsymbol{0} & \boldsymbol{0} & \boldsymbol{0} & \boldsymbol{0} \\ & & \vdots & & \\ \boldsymbol{0} & \boldsymbol{0} & \boldsymbol{0} & \boldsymbol{0} & \boldsymbol{H}_n \\ \overleftarrow{\boldsymbol{H}}_{12} & \overrightarrow{\boldsymbol{H}}_{12} & \boldsymbol{0} & \boldsymbol{0} & \boldsymbol{0} \\ & & \vdots & & \\ \boldsymbol{0} & \boldsymbol{0} & \boldsymbol{0} & \overleftarrow{\boldsymbol{H}}_{(n-1)n} & \overrightarrow{\boldsymbol{H}}_{(n-1)n} \end{bmatrix} \tag{10}$$

For the part of absolute observations, $\boldsymbol{H}_i = \left.\frac{\delta \boldsymbol{h}_i}{\delta \boldsymbol{x}_i}\right|_{\boldsymbol{x}_i = \hat{\boldsymbol{x}}_i}$ corresponds to the Jacobian matrix in the pseudorange single point positioning process. As for the relative measurements, $\overleftarrow{\boldsymbol{H}}_{ij} = \left.\frac{\delta \boldsymbol{h}_{ij}}{\delta \boldsymbol{x}_i}\right|_{\boldsymbol{x}_i = \hat{\boldsymbol{x}}_i, \boldsymbol{x}_j = \hat{\boldsymbol{x}}_j}$ and $\overrightarrow{\boldsymbol{H}}_{ij} = \left.\frac{\delta \boldsymbol{h}_{ij}}{\delta \boldsymbol{x}_j}\right|_{\boldsymbol{x}_i = \hat{\boldsymbol{x}}_i, \boldsymbol{x}_j = \hat{\boldsymbol{x}}_j}$ denote the linearized observation matrices correspond to $\boldsymbol{x}_i$ and $\boldsymbol{x}_j$ respectively. Since a relative measurement is assumed to be available to both UAVs, we can have $\overleftarrow{\boldsymbol{H}}_{ij} = -\overrightarrow{\boldsymbol{H}}_{ij}$.

To be more specific, the observation matrix $\overleftarrow{\boldsymbol{H}}_{ij}$ for three-dimensional relative measurement $\boldsymbol{z}_{ij}$ can be formed as:

$$\overleftarrow{\boldsymbol{H}}_{ij} = \begin{bmatrix} -\boldsymbol{I}_{3\times 3} & \boldsymbol{0}_{3\times 4} \end{bmatrix} \tag{11}$$

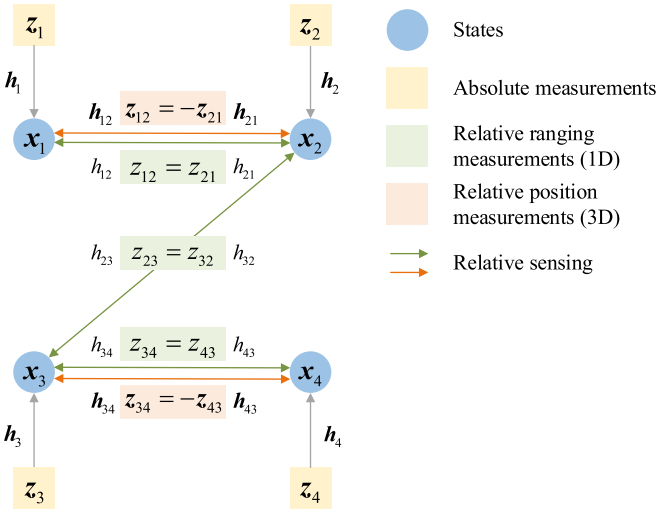

Fig. 1. State and measurement graph in an example of a multi-UAV system.

The observation matrix $\overleftarrow{\boldsymbol{H}}_{ij}$ for one-dimensional relative measurement z_{ij} is formed by:

$$\overleftarrow{\boldsymbol{H}}_{ij} = \begin{bmatrix} -\boldsymbol{e}_{ij} & \boldsymbol{0}_{1\times 4} \end{bmatrix} \tag{12}$$

where $\boldsymbol{e}_{ij} = \begin{bmatrix} x_j^{\mathrm{E}} - x_i^{\mathrm{E}} & x_j^{\mathrm{N}} - x_i^{\mathrm{N}} & x_j^{\mathrm{U}} - x_i^{\mathrm{U}} \end{bmatrix}$ is the normalized Line-of-Sight (LOS) vector from the UAV i to UAV j.

Then, the state vector $\boldsymbol{X}$ in (9) can be estimated by Weighted Least-Squares (WLS). The update for $\Delta\hat{\boldsymbol{X}}$ at each iteration is given by:

$$\Delta\hat{\boldsymbol{X}} = \left(\boldsymbol{H}^{\mathrm{T}}\boldsymbol{W}\boldsymbol{H}\right)^{-1}\boldsymbol{H}^{\mathrm{T}}\boldsymbol{W} \cdot \Delta\boldsymbol{Z} \tag{13}$$

where $\Delta\boldsymbol{Z}$ is the vector of the measurements minus the expected ranging values, and the observations are weighted by the diagonal matrix $\boldsymbol{W}$.

The weighting matrix $\boldsymbol{W}$ is determined by the covariance matrix $\boldsymbol{C}$ associated with the measurements:

$$\boldsymbol{W}(r, r) = \left(\boldsymbol{C}(r, r)\right)^{-1}, r = 1, 2, \ldots \tag{14}$$

$$\boldsymbol{C} = \mathrm{blkdiag}\left([\boldsymbol{C}_1, \cdots, \boldsymbol{C}_n, \boldsymbol{C}_{12}, \cdots, \boldsymbol{C}_{(n-1)n}]\right) \tag{15}$$

where $\boldsymbol{C}_i = \mathrm{diag}[(\sigma_i^1)^2, (\sigma_i^2)^2, \cdots, (\sigma_i^{N_i})^2]$ corresponds to the pseudorange observations, $\boldsymbol{C}_{ij}$ is equal to the associated variance relative measurement, i.e., σ_{uwb}^2 and σ_{RP}^2.

The covariance matrix of the estimated states, i.e., $\boldsymbol{C}_{\boldsymbol{X}} = \mathrm{blkdiag}([\boldsymbol{C}_{\boldsymbol{x}_1}, \cdots, \boldsymbol{C}_{\boldsymbol{x}_n}])$ can be calculated as:

$$\boldsymbol{C}_{\boldsymbol{X}} = \boldsymbol{S} \cdot \boldsymbol{C} \cdot \boldsymbol{S}^{\mathrm{T}} \tag{16}$$

$$\boldsymbol{S} = \left(\boldsymbol{H}^{\mathrm{T}}\boldsymbol{W}\boldsymbol{H}\right)^{-1}\boldsymbol{H}^{\mathrm{T}}\boldsymbol{W} \tag{17}$$

Fig. 1 presents an example of a multi-UAV system with 4 agents, and shows the states and the graph of absolute and relative measurements. Taking the system as an example, two different centralized structures are shown by Fig. 2, i.e., the fully-centralized structure and the locally-centralized structure. For the fully-centralized one, all the states in the system are estimated together in one single fusion center by employing all the information. With respect to the locally-centralized structure, UAVs are separated into different clusters, each of which has a fusion center and utilizes a subset of the information to estimate the states of the UAVs.

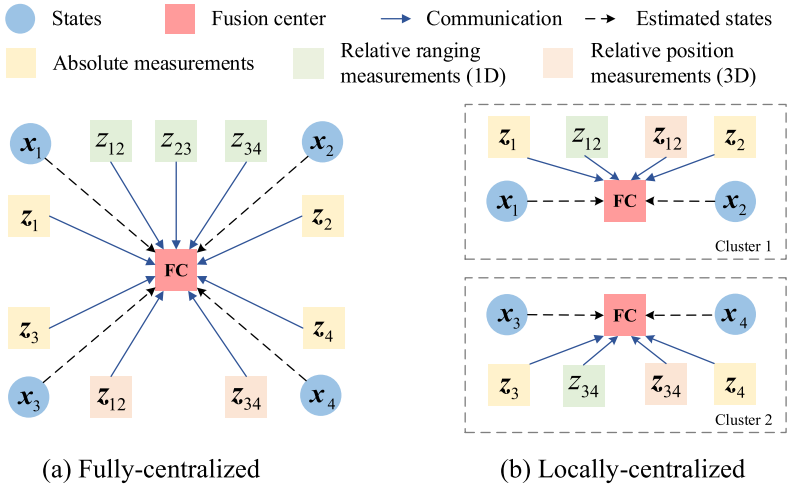

Fig. 2. Two different centralized CN structures for the above example.

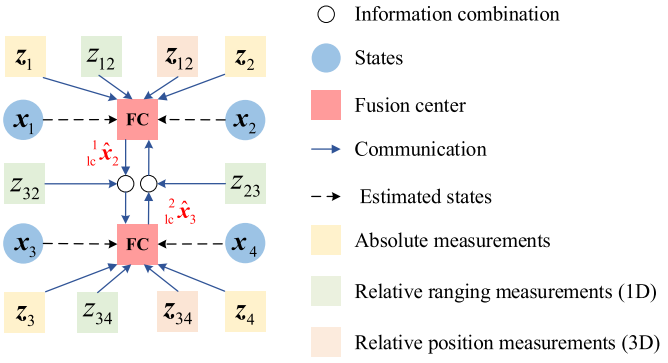

Fig. 3. Distributed clustering CN structure corresponding to the above multi-UAV system.

3.2. Least squares based distributed clustering CN

Based on the locally-centralized structure for separate clusters, a distributed clustering structure is proposed in this section. The matrices under the locally-centralized architecture have been given by Equations (9) to (17). We re-label these variables as ${}^{i}\boldsymbol{X}$, ${}^{i}_{\text{lc}}\boldsymbol{Z}$, ${}^{i}_{\text{lc}}\boldsymbol{H}$, ${}^{i}_{\text{lc}}\boldsymbol{W}$, ${}^{i}_{\text{lc}}\hat{\boldsymbol{X}}$, ${}^{i}_{\text{lc}}\boldsymbol{C}$, ${}^{i}_{\text{lc}}\boldsymbol{S}$, ${}^{i}_{\text{lc}}\boldsymbol{C}_{\boldsymbol{X}}$ respectively, where the subscript lc indicates the locally-centralized structure and i represents the cluster. Each UAV can preliminarily obtain a state estimate from the locally-centralized structure. The communication links and the inter-cluster relative measurements can be explored for further estimation performance enhancement.

The structure shown in Fig. 3 corresponds to the aforementioned system. As seen, there exist communication link and relative measurement between the UAV 2 in Cluster 1 and the UAV 3 in Cluster 2. Therefore, Cluster 1 receives the state estimate ${}^{2}_{\text{lc}}\hat{\boldsymbol{x}}_3$ with relative ranging measurement z_{23} from the other cluster. The state estimates can serve as the observations in the distributed CN structure for separate clusters.

In general, for the distributed structure of cluster i, the combination of the state estimates and relative measurements are as follows:

$$\begin{bmatrix} {}^{i}_{\text{lc}}\hat{\boldsymbol{x}}_{i_1} \\ \vdots \\ {}^{i}_{\text{lc}}\hat{\boldsymbol{x}}_{i_n} \\ \boldsymbol{z}_{i_1 j_1} \\ \vdots \end{bmatrix} = \begin{bmatrix} {}^{i}\boldsymbol{x}_{i_1} \\ \vdots \\ {}^{i}\boldsymbol{x}_{i_n} \\ \boldsymbol{h}^{i_1}_{i_1 j_1}({}^{i}\boldsymbol{x}_{i_1}) \\ \vdots \end{bmatrix} + \begin{bmatrix} \boldsymbol{v}_{i_1} \\ \vdots \\ \boldsymbol{v}_{i_n} \\ \boldsymbol{v}_{i_1 j_1} \\ \vdots \end{bmatrix} \tag{18}$$

where $i_1, \cdots, i_n$ are the UAVs whose states are estimated in cluster i. The existence of $\boldsymbol{z}_{i_1 j_1}$ indicates that there exists relative sensing link with other clusters. $\boldsymbol{z}_{i_1 j_1}$ is sent together with the locally-centralized estimate ${}^{j}_{\text{lc}}\hat{\boldsymbol{x}}_{j_1}$ to the fusion center of cluster i, and $\boldsymbol{h}^{i_1}_{i_1 j_1}$ denotes the nonlinear function of ${}^{i}\boldsymbol{x}_{i_1}$.

By linearizing $\boldsymbol{h}^{i_1}_{i_1 j_1}$ at the updated estimate in distributed structure, i.e., ${}^{i}\boldsymbol{x}_{i_1} = {}^{i}_{\text{d}}\hat{\boldsymbol{x}}_{i_1}$, (18) can be formed as:

$${}^{i}_{\text{d}}\boldsymbol{Z} = {}^{i}_{\text{d}}\boldsymbol{H}\,{}^{i}\boldsymbol{X} + {}^{i}_{\text{d}}\boldsymbol{V} \tag{19}$$

where the subscript d indicates the distributed structure.

The observation matrix ${}^{i}_{\text{d}}\boldsymbol{H}$ is given as:

$${}^{i}_{\text{d}}\boldsymbol{H} = \begin{bmatrix} {}^{i}_{\text{d}}\boldsymbol{H}_{i_1} & \boldsymbol{0} & \cdots & \boldsymbol{0} & \boldsymbol{0} \\ & & \vdots & & \\ \boldsymbol{0} & \boldsymbol{0} & \cdots & \boldsymbol{0} & {}^{i}_{\text{d}}\boldsymbol{H}_{i_n} \\ {}^{i}_{\text{d}}\overleftarrow{\boldsymbol{H}}^{i_1}_{i_1 j_1} & \boldsymbol{0} & \cdots & \boldsymbol{0} & \boldsymbol{0} \\ & & \vdots & & \end{bmatrix} \tag{20}$$

where ${}^{i}_{\text{d}}\boldsymbol{H}_{i_m} = \text{blkdiag}\left(\begin{bmatrix} \boldsymbol{I}_{3\times 3} & \boldsymbol{0}_{3\times 4} \end{bmatrix}\right)$, and ${}^{i}_{\text{d}}\overleftarrow{\boldsymbol{H}}^{i_m}_{i_m j_m} = \text{blkdiag}\left(\begin{bmatrix} -\boldsymbol{I}_{3\times 3} & \boldsymbol{0}_{3\times 4} \end{bmatrix}\right)$. As for relative ranging information, the corresponding matrix will be ${}^{i}_{\text{d}}\overleftarrow{\boldsymbol{H}}^{i_m}_{i_m j_m} = \begin{bmatrix} -({}^{j}_{\text{lc}}\hat{\boldsymbol{x}}^{\text{T}}_{j_m} - {}^{i}_{\text{d}}\hat{\boldsymbol{x}}^{\text{T}}_{i_m})/z_{i_m j_m} & \boldsymbol{0}_{1\times 4} \end{bmatrix}$.

The state vector ${}^{i}\boldsymbol{X}$ can be estimated by WLS, with the update for $\Delta^{i}_{\text{d}}\hat{\boldsymbol{X}}$ at each iteration given by (9) and the weighting matrix ${}^{i}_{\text{d}}\boldsymbol{W}$ given by (14). The covariance matrix ${}^{i}_{\text{d}}\boldsymbol{C}$ is a diagonal matrix decided by the covariance matrix of each observation:

$${}^{i}_{\text{d}}\boldsymbol{C} = \text{blkdiag}\left(\begin{bmatrix} {}^{i}_{\text{lc}}\boldsymbol{C}_{\boldsymbol{X}} & \boldsymbol{C}^{i_1}_{i_1 j_1} & \cdots & \boldsymbol{C}^{i_n}_{i_n j_n} \end{bmatrix}\right) \tag{21}$$

where ${}^{i}_{\text{lc}}\boldsymbol{C}_{\boldsymbol{X}} = \text{blkdiag}([{}^{i}_{\text{lc}}\boldsymbol{C}_{\boldsymbol{x}_{i_1}}, \cdots, {}^{i}_{\text{lc}}\boldsymbol{C}_{\boldsymbol{x}_{i_n}}])$ is obtained by (16) and (17). The covariance matrix $\boldsymbol{C}^{i_m}_{i_m j_m}$ is given as:

$$\boldsymbol{C}^{i_m}_{i_m j_m} = \boldsymbol{\sigma}^2_{\text{RP}} + {}^{j}_{\text{lc}}\boldsymbol{C}_{\boldsymbol{x}_{j_m}} \tag{22}$$

As for inter-cluster relative ranging measurement, the covariance matrix $C^{i_m}_{i_m j_m}$ will be computed as:

$$C^{i_m}_{i_m j_m} = \sigma^2_{\text{uwb}} + \boldsymbol{e}_{i_m j_m} \cdot {}^{j}_{\text{lc}}\boldsymbol{C}_{\boldsymbol{x}_{j_m}} \cdot \boldsymbol{e}^{\text{T}}_{i_m j_m} \tag{23}$$

The covariance matrix of the estimated states, i.e., ${}^{i}_{\text{d}}\boldsymbol{C}_{\boldsymbol{X}} = \text{blkdiag}([{}^{i}_{\text{d}}\boldsymbol{C}_{\boldsymbol{x}_{i_1}}, \cdots, {}^{i}_{\text{d}}\boldsymbol{C}_{\boldsymbol{x}_{i_n}}])$ can be calculated as:

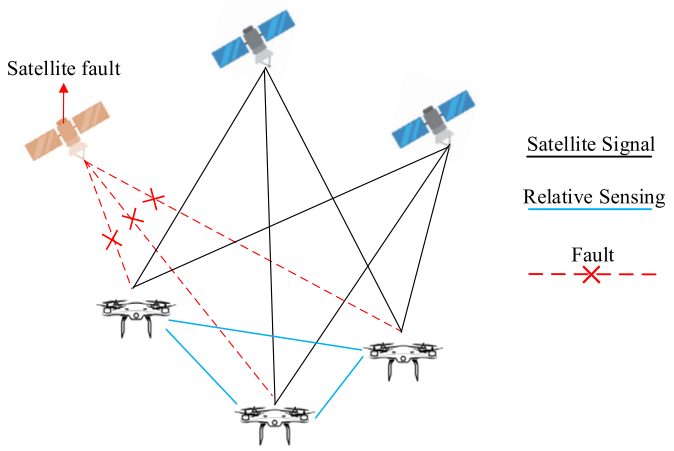

Fig. 4. Satellite fault mode in CN system.

$$ {}^{i}_{\mathrm{d}}\boldsymbol{C}_{\boldsymbol{X}} = {}^{i}_{\mathrm{d}}\boldsymbol{S} \cdot {}^{i}_{\mathrm{d}}\boldsymbol{C} \cdot {}^{i}_{\mathrm{d}}\boldsymbol{S}^{\mathrm{T}} \tag{24} $$

$$ {}^{i}_{\mathrm{d}}\boldsymbol{S} = \left({}^{i}_{\mathrm{d}}\boldsymbol{H}^{\mathrm{T}} \cdot {}^{i}_{\mathrm{d}}\boldsymbol{W} \cdot {}^{i}_{\mathrm{d}}\boldsymbol{H}\right)^{-1} \cdot {}^{i}_{\mathrm{d}}\boldsymbol{H}^{\mathrm{T}} \cdot {}^{i}_{\mathrm{d}}\boldsymbol{W} \tag{25} $$

3.3. Fusion architecture comparison

Three different CN architectures are presented in Section 3.1 and Section 3.2: (1) fully-centralized structure for the whole system, (2) locally-centralized structure for clusters, and (3) distributed structure based on locally-centralized estimates in separate clusters. The comparison among these three categories of fusion structures is analyzed as follows:

(1) On one hand, the fully-centralized structure employs all the measurements in the system, so the obtained solution must be global optimal in accuracy. On the other hand, it requires a large amount of bandwidth to send raw data. Moreover, the computational cost is high and the reliability is poor.
(2) By clustering the system, the locally-centralized structure can reduce the computational cost. However, the accuracy is decreased comparing to the fully-centralized one and some inter-cluster relative measurements are not utilized in the system.
(3) Based on the estimates obtained in the locally-centralized structure, the communication links and the inter-cluster relative measurements are explored for estimation performance enhancement. As a result, the distributed structure among clusters provides better accuracy, robustness and flexibility.

4. Fault detection and exclusion algorithm for multi-UAV cluster-based CN

This section develops an FDE scheme for the multi-UAV cluster-based CN system. Section 4.1 lists the fault modes that might happen in a multi-UAV formation. Then, Section 4.2 and Section 4.3 introduce the FDE algorithm corresponding to the locally-centralized clustering structure and the distributed clustering structure.

4.1. Fault modes

GNSS-based cooperative navigation system utilizes pseudorange measurements and relative measurements, which may be affected by interferences with severe errors induced [11]. In this circumstance, the fault should be detected and excluded, which calls for an FDE algorithm.

In this paper, two basic fault modes are considered to cover different fault scenarios in a CN system: (a) the satellite fault which affects pseudorange measurements as shown in Fig. 4, and (b) the node fault which affects relative measurements as shown in Fig. 5. From the perspective of sensors, relative measurements can be divided into P2P ranging and relative positions. In terms of fusion structures, relative measurements can be divided into intra-cluster measurements and inter-cluster measurements, which are separately employed in locally-centralized clustering CN and distributed CN.

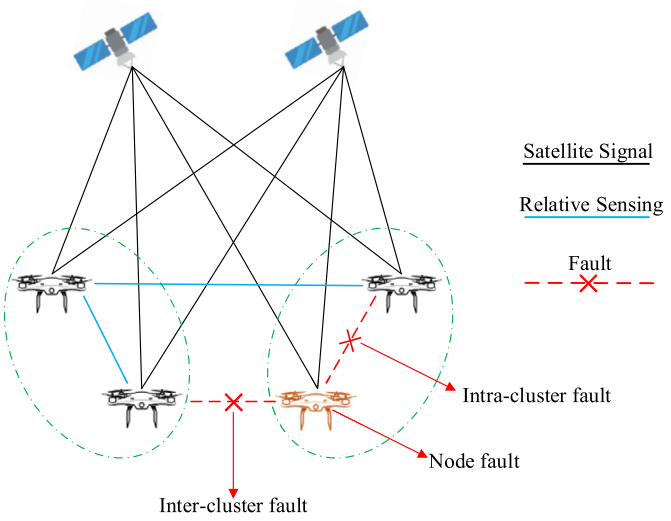

Fig. 5. Node fault mode in CN system.

4.2. Fault detection for locally-centralized clustering CN based on solution separation

FDE can be divided into two steps: Fault Detection (FD) and Fault Exclusion (FE). Based on the solution separation method, the FD process for locally-centralized clustering CN is described in detail as follows.

The measurements include pseudorange observations and relative measurements, which can be separated into different subsets to reduce the computation load. For each subset k, the difference $\Delta^{i}_{\mathrm{lc}}\hat{\boldsymbol{X}}^{(k)}$ between the fault-tolerant solution ${}^{i}_{\mathrm{lc}}\hat{\boldsymbol{X}}^{(k)}$ and the all-in-view solution ${}^{i}_{\mathrm{lc}}\hat{\boldsymbol{X}}^{(0)}$, the standard deviations, and the test thresholds are determined as follows [26].

For subset k, the diagonal weighting matrix is computed as:

$$ {}^{i}_{\mathrm{lc}}\boldsymbol{W}^{(k)}(j,j) = \begin{cases} {}^{i}_{\mathrm{lc}}\boldsymbol{W}(j,j), & \text{if } {}^{i}_{\mathrm{lc}}\boldsymbol{Z}(j) \text{ is assumed healthy} \\ 0, & \text{otherwise} \end{cases} \tag{26} $$

The statistic for subset k, i.e., $\Delta^{i}_{\mathrm{lc}}\hat{\boldsymbol{X}}^{(k)}$, is computed as:

$$ \Delta^{i}_{\mathrm{lc}}\hat{\boldsymbol{X}}^{(k)} = {}^{i}_{\mathrm{lc}}\hat{\boldsymbol{X}}^{(k)} - {}^{i}_{\mathrm{lc}}\hat{\boldsymbol{X}}^{(0)} = \left({}^{i}_{\mathrm{lc}}\boldsymbol{S}^{(k)} - {}^{i}_{\mathrm{lc}}\boldsymbol{S}^{(0)}\right)\boldsymbol{Y} \tag{27} $$

where $\boldsymbol{Y}$ is the vector of measurements minus the expected range for an all-in-view position solution, and it is equal to the last $\Delta^{i}_{\mathrm{lc}}\boldsymbol{Z}$ in (13) when the solution has converged. And the coefficient matrixes ${}^{i}_{\mathrm{lc}}\boldsymbol{S}^{(0)}$ and ${}^{i}_{\mathrm{lc}}\boldsymbol{S}^{(k)}$ are given by (17).

For each cluster, let the index $q = 1$, 2, and 3 designate the east, north, and up components of each UAVs in the cluster. The variance $\sigma^{(k)2}_{i_m,q}$ of the difference $\Delta^{i}_{\mathrm{lc}}\hat{\boldsymbol{x}}^{(k)}_{i_m,q}$ between the all-in-view and the fault-tolerant position solutions is given as:

$$ \sigma^{(k)2}_{i_m,q} = \boldsymbol{e}^{\mathrm{T}}_{i_m,q}\left({}^{i}_{\mathrm{lc}}\boldsymbol{S}^{(k)} - {}^{i}_{\mathrm{lc}}\boldsymbol{S}^{(0)}\right){}^{i}_{\mathrm{lc}}\boldsymbol{C}\left({}^{i}_{\mathrm{lc}}\boldsymbol{S}^{(k)} - {}^{i}_{\mathrm{lc}}\boldsymbol{S}^{(0)}\right)^{\mathrm{T}}\boldsymbol{e}_{i_m,q} \tag{28} $$

where i_m is the UAV index in cluster i, $\boldsymbol{e}_{i_m,q}$ represents a vector in which $[7 \cdot (i_m - 1) + q]$th entry is 1 and the others are 0.

For each subset, the thresholds indexed by UAV index i_m, fault subset index k and coordinate index q are given as:

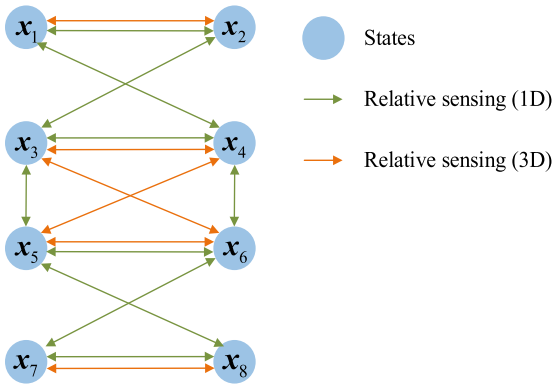

Fig. 6. State and relative sensing graph of the simulated multi-UAV system.

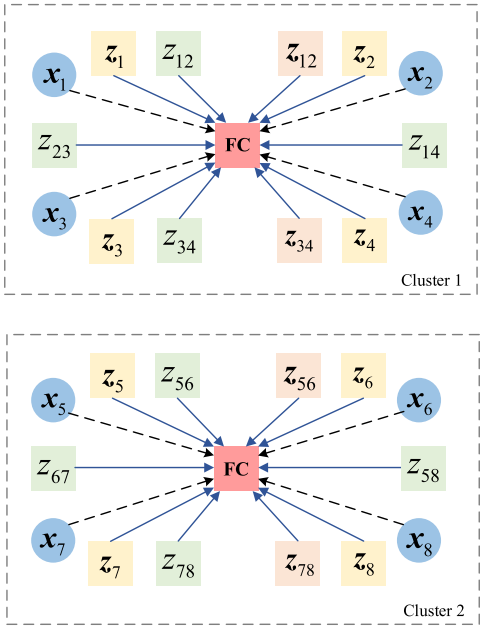

Fig. 7. The locally-centralized structure and clusters of the system.

$$T_{i_m,q}^{(k)} = \boldsymbol{K}_{fa,q}\sigma_{i_m,q}^{(k)} \tag{29}$$

where $\boldsymbol{K}_{fa,q}$ is a factor related to false alarm rate [26].

Then, the threshold tests are carried out with the solution separation residual computed as:

$$\tau_{i_m,q}^{(k)} = \frac{|{}_{\text{lc}}^{i}\hat{\boldsymbol{x}}_{i_m,q}^{(k)} - {}_{\text{lc}}^{i}\hat{\boldsymbol{x}}_{i_m,q}^{(0)}|}{T_{i_m,q}^{(k)}} \leq 1 \tag{30}$$

If any of the tests fails, FD raises the fault alert and FE must be attempted.

4.3. FE scheme for locally-centralized clustering CN

FE aims to find out which subset solution can exclude the faulty measurements exactly. In terms of solution separation method, Blanch et al. have shown that the subset with the largest solution separation residual is a good choice for exclusion [26]. To seek a fault-free subset, a set of measurements of size N_{ex} need to be excluded. For each possible value of N_{ex}, from 1 to $N_{f,max}$, the best candidate subset for exclusion is determined by [11]:

$$k_{N_{ex}} = \underset{k}{argmax}\{\tau_{i_m,q}^{(k)} \mid N_f^{(k)} = Nex\} \tag{31}$$

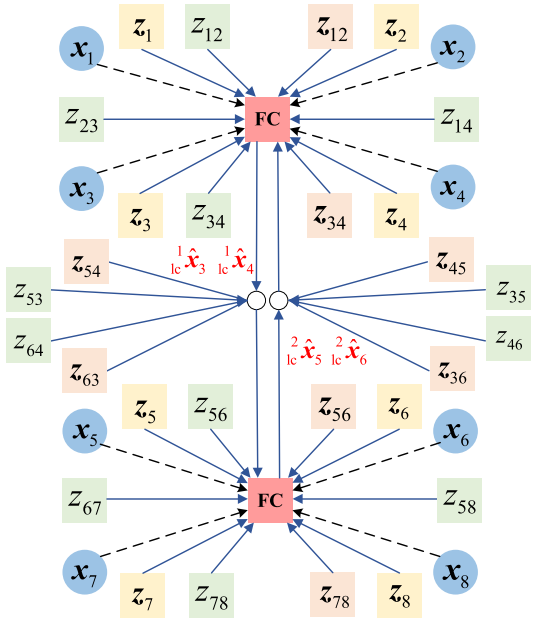

Fig. 8. The distributed clustering structure of the system.

where $N_f^{(k)}$ denotes the number of the measurements assumed faulted. Note that, if measurements are grouped, each group is regarded as an individual "measurement" when calculating $N_f^{(k)}$ and N_{ex}.

The subset candidate $k_{N_{ex}}$ should be checked further. Let us define $k_{N_{ex}}$ as the new all-in-view set. Then the FD process will be performed for the new set. If the solution separation tests pass, the new all-in-view solution will be the expected fault-free solution.

4.4. FDE scheme for distributed clustering CN

The FDE algorithm for distributed clustering CN can be derived based on Section 3.2 and Section 4.1 and Section 4.2. By replacing the relevant variables in Equations (26) to (31) as ${}_{\text{d}}^{i}\hat{\boldsymbol{X}}^{(\cdot)}$, ${}_{\text{d}}^{i}\boldsymbol{W}^{(\cdot)}$, ${}_{\text{d}}^{i}\boldsymbol{S}^{(\cdot)}$, ${}_{\text{d}}^{i}\boldsymbol{Z}$, and ${}_{\text{d}}^{i}\hat{\boldsymbol{x}}_{i_m,q}^{(k)}$, we can have the corresponding process of the FDE for the distributed structure. Compared with the locally-centralized structure, the FDE scheme for distributed clustering CN focuses on the fault of inter-cluster relative measurements.

5. Simulation results

Section 5.1 introduces the simulation configurations. Subsequently, MATLAB-based simulations are carried out in Section 5.2 to preliminary evaluate the performance of the proposed clustering CN structures and the FDE capability. Furthermore, Spirent simulator is adopted in Section 5.3 to simulate the urban environment for a more realistic multipath scenario.

5.1. Simulation configurations

A MATLAB-based simulation platform for an 8-UAV system navigation performance evaluation is established. The system is presented in Fig. 6, with the locally-centralized clustering structure and distributed clustering structure shown as Fig. 7 and Fig. 8. Monte-Carlo simulations are conducted to generate 1000 random scenarios, which are used to statistically determine the error standard deviations. Table 1 shows the descriptions of the three methods simulated for comparison and validation. Pseudorange and relative measurements are simulated by white Gaussian noise with

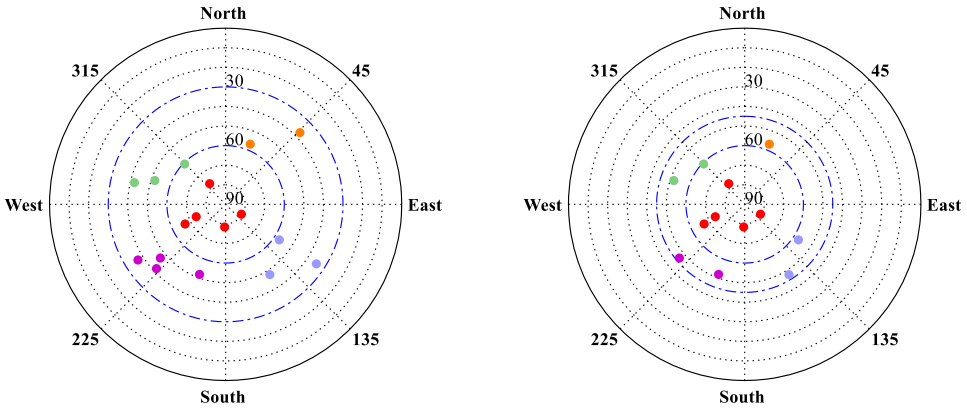

(a) Mask angle = 30° (open sky) (b) Mask angle = 45° (urban)

Fig. 9. The grouping result for the satellites (Each color represents a group). (For interpretation of the colors in the figure(s), the reader is referred to the web version of this article.)

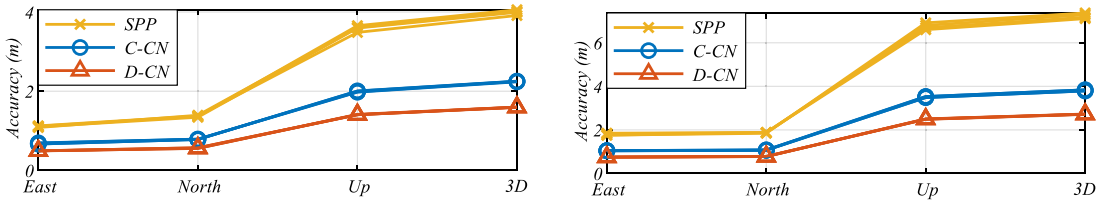

(a) Open sky (b) Urban

Fig. 10. Accuracy comparison among the three methods.

Table 1
Descriptions for the methods compared.

Method	Measurements	Label
Single Point Positioning	Pseudorange	SPP
Locally-centralized Clustering CN	Pseudorange Intra-cluster relative measurements	C-CN
Distributed Clustering CN	Estimated states Inter-cluster relative measurements	D-CN

Table 2
Standard deviations of the measurement errors.

Measurements	Standard deviation of the error (m)		
	Fault-Free	Intra-cluster Fault	Inter-cluster Fault
Pseudorange	2	20	
P2P ranging	0.2	20	
Relative Position	[0.1, 0.1, 0.1]	[20, 20, 20]	

standard deviations listed in Table 2, including fault-free and fault scenarios.

For the satellites, the mask angle is set at 30° and 45° to simulate two scenarios: (a) open sky, and (b) urban environments. According to the spatial correlation of the faults in satellites, fault grouping is adapted here by dividing the low-elevation satellites into several non-overlapping groups [31]. The grouping results for the visible satellites are shown in Fig. 9. The grouping process follows the criteria that the neighboring satellites should be divided into two subsets if their azimuths differ by more than 45°.

5.2. Simulation for performance evaluation

First, we analyze the accuracy of these two CN architectures, i.e., the locally-centralized clustering CN and the distributed clustering CN, compared with the traditional GNSS-only method, i.e., Single Point Positioning (SPP). The position results of these UAVs are shown in Fig. 10. For the reason that all UAVs share the same visible satellites and environments, there is little difference among

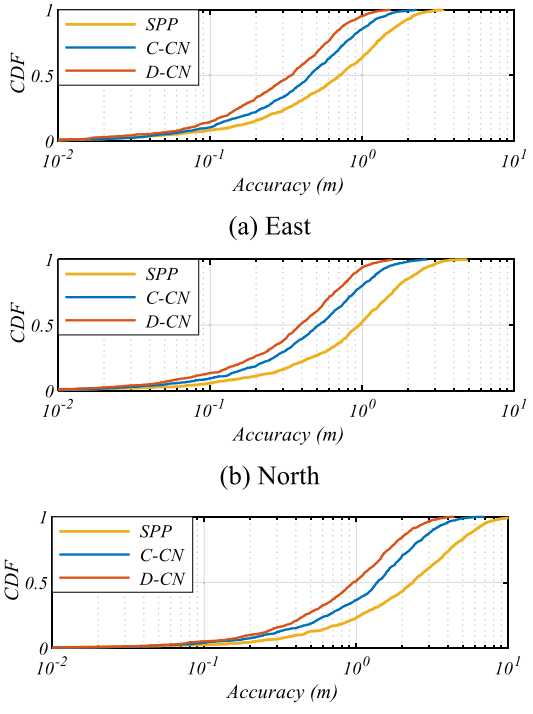

(a) East (b) North (c) Up

Fig. 11. A comprehensive performance comparison among the three methods.

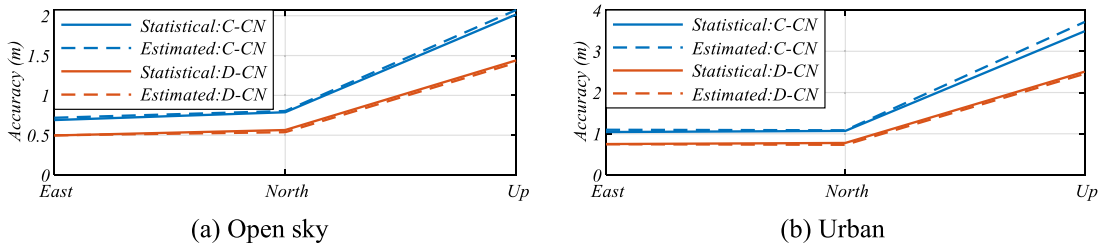

Fig. 12. The statistical (solid lines) and estimated (dashed lines) error standard deviations.

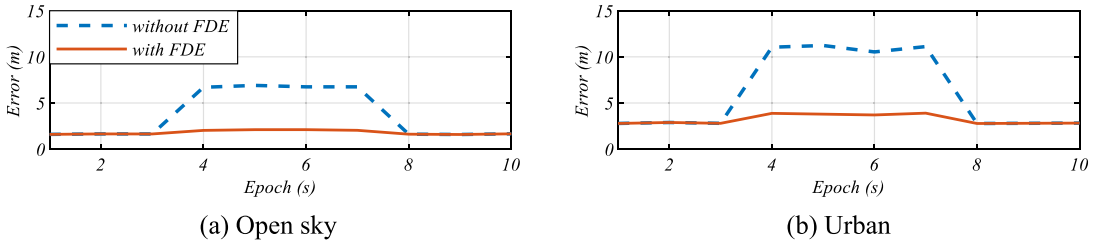

Fig. 13. The comparison between the positioning errors with and without FDE (Satellite fault).

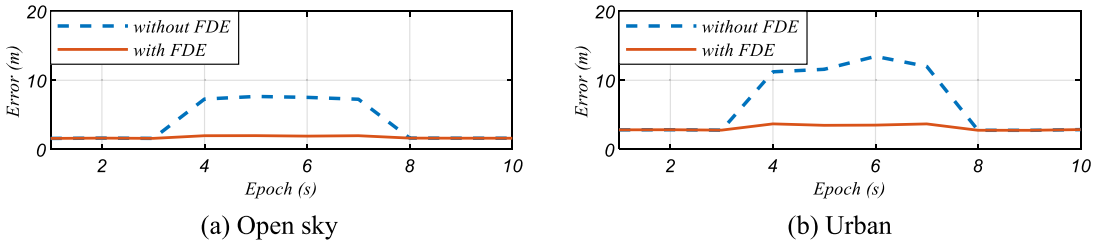

Fig. 14. The comparison between the positioning errors with and without FDE (Node fault on intra-cluster P2P ranging).

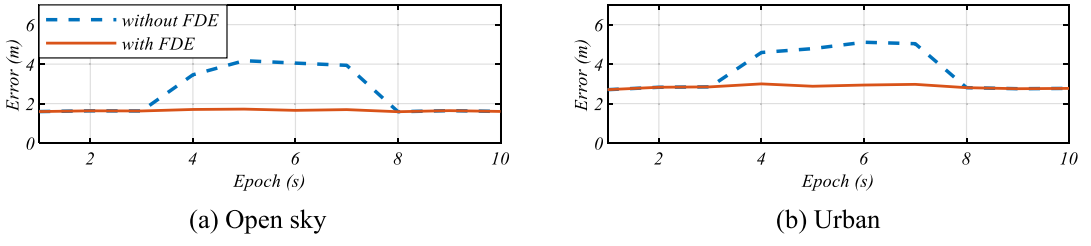

Fig. 15. The comparison between the positioning errors with and without FDE (Node fault on intra-cluster relative position).

the accuracy of the solutions. In open sky, the locally-centralized clustering CN provides a 43.91% improvement in positioning accuracy, while the distributed clustering CN improves about 59.23%. In urban areas, it can be seen that the accuracy of GNSS-only method is degraded. In this circumstance, the performance of GNSS-only method is improved about 47.92% by the locally-centralized clustering CN, and the distributed clustering CN improves the accuracy about 63.09%. Therefore, the accuracy can be effectively improved by these two proposed CN methods for multi-UAV systems, especially in urban navigation applications.

Fig. 11 gives a direct view of the performance comparison among the three methods. Accuracy is presented in the form of Cumulative Distribution Function (CDF), which specifies the probability or normalized frequency that a variable X takes a value less than or equal to a given value x. It shows that the distributed clustering CN can effectively improve the performance of the locally-centralized clustering CN by exploiting the inter-cluster relative measurements. Then, Fig. 12 presents the statistical and estimated error standard deviations in different environments, which effectively validates the covariance model.

Table 3
Error modes considered in simulation.

Fault Mode	Measurement	
Satellite Fault	Pseudorange	
Node Fault	P2P ranging	Intra-cluster Inter-cluster
	Relative Position	Intra-cluster Inter-cluster

Additionally, in order to validate the performance of the proposed FDE algorithm, we perform the simulations with fault introduced into the measurements from 4s to 7s and compare the positioning errors with FDE the results without FDE. For each second, Monte-Carlo simulations are conducted to generate 1000 random scenarios. The simulated error modes are listed in Table 3.

Fig. 13 to 17 present the accuracy comparison in 3D direction. It is shown that the FDE scheme can significantly reduce the error in different fault modes and different fusion architectures. The results

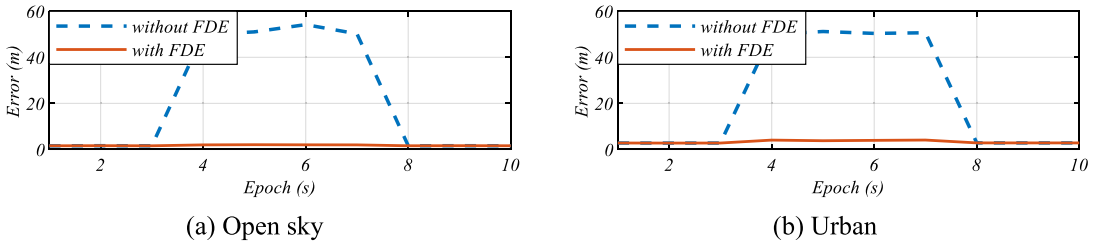

Fig. 16. The comparison between the positioning errors with and without FDE (Node fault both on intra-cluster and inter- cluster P2P ranging).

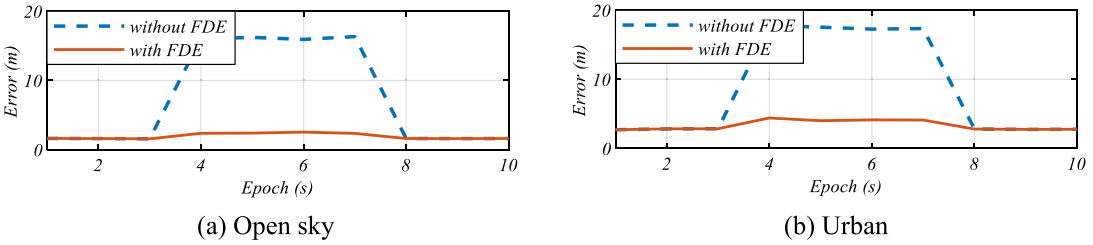

Fig. 17. The comparison between the positioning errors with and without FDE (Node fault both on intra-cluster and inter- cluster relative position).

Fig. 18. The simulated trajectory (red line) in the Shanghai city model of the Spirent simulator.

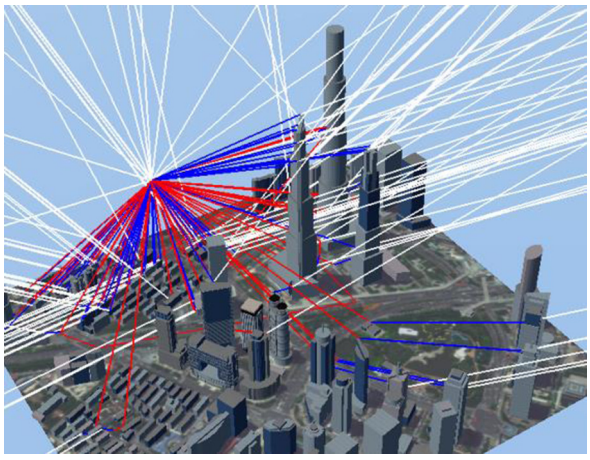

Fig. 19. The visualization of the multipath in urban area provided by the Spirent Sim3D.

suggest that the faults are detected and excluded correctly by the proposed FDE for multi-UAV CN.

5.3. Simulation based on the Spirent simulator for multipath scenario

In order to simulate a more realistic multipath scenario for the FDE scheme, the Spirent GSS7000 GNSS simulator running the Spirent SimGEN software is utilized for pseudorange observations. It enables receiver performance test in a controlled laboratory setting that is otherwise impossible with live GNSS signals [33]. To further simulate urban scenario, the Spirent Sim3D software is adopted. Sim 3D can realize multipath and NLOS simulation using the ray tracing technique, which provides a realistic real-time multipath simulation environment and signal reflection visualization function [34]. An SinoGNSS M300 Pro receiver is used to receive the simulated signals and restore the rinex files.

Considering a city aerial surveillance task conducted by 4 UAVs, we design a trajectory around a block as shown by Fig. 18. We assume that these UAVs fly along the trajectory in a counterclockwise direction with different starting points. The visualization of the multipath in urban area provided by the Spirent Sim3D is presented in Fig. 19. The heights of these 4 UAVs are respectively set to 400 m, 350 m, 250 m and 200 m. Fig. 20 presents the visible satellites.

Pseudorange is affected by satellite clock/orbit bias, atmospheric delay, receiver thermal noise and multipath effects [35]. Most of the errors can be eliminated by DGNSS based on the principle that those error sources are differentiable between the GNSS reference station and UAVs [36]. Therefore, the pseudorange observations have been corrected through DGNSS by setting a base station. According to the statistics of the corrected pseudorange, the standard deviation of the error is about 3 m.

The error comparison in a multipath-free scenario in 3D direction between SPP and the proposed CN scheme is shown by Fig. 21, which preliminary reveals the improvement provided by the multi-UAV CN algorithm. Then, with the multipath scenario introduced, Fig. 22 shows that the clustering CN structure is heavily affected by the fault, revealing the necessity of developing an FDE scheme for the proposed CN architecture in complex areas. Further, the results shown in Fig. 23 illustrate that the fault caused by multipath can be detected and excluded correctly by the proposed FDE in the urban environment.

6. Conclusions and future work

This paper has described two categories of cluster-based fusion architectures, i.e., the locally-centralized structure and the dis-

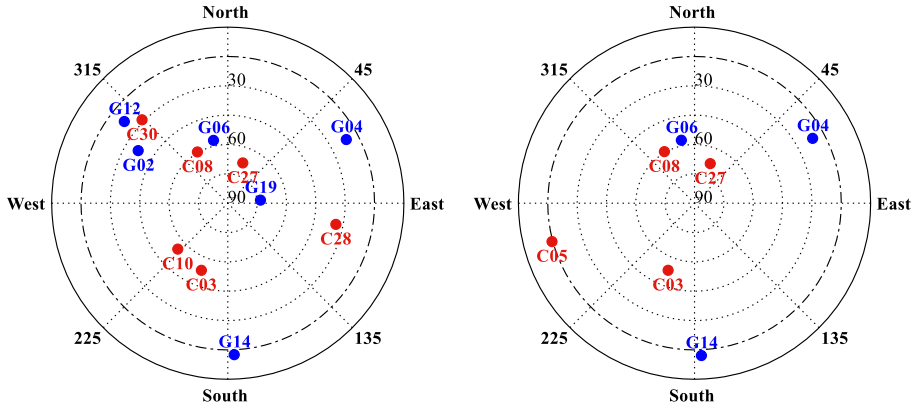

(a) UAV at 400m (b) UAV at 200m

Fig. 20. The visible satellites of the simulated UAVs.

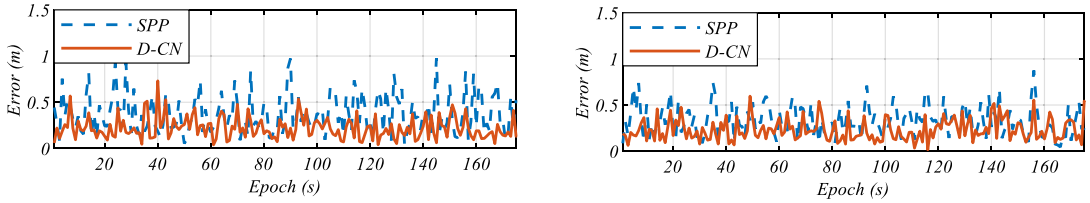

(a) UAV at 400m (b) UAV at 200m

Fig. 21. Error comparison between the SPP method and the proposed CN in a multipath-free scenario.

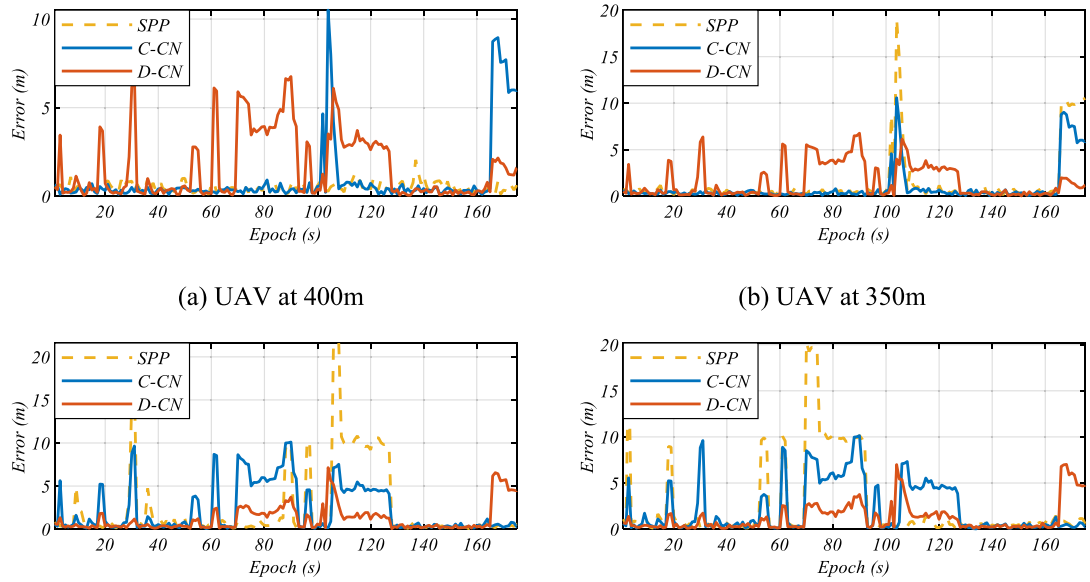

(a) UAV at 400m (b) UAV at 350m

(c) UAV at 250m (d) UAV at 200m

Fig. 22. Error comparison between the SPP method and the proposed CN in the multipath scenario.

tributed structure, and has proposed a corresponding FDE scheme. It has been demonstrated that the proposed cluster-based CN can effectively improve the positioning accuracy, especially in urban areas. Further, it has been shown that the proposed FDE scheme under these two fusion structures can significantly help in different fault scenarios. This framework achieves the balance between efficiency and accuracy, and improves navigation reliability in GNSS-challenging scenario.

Moreover, the cluster-based architecture can generally represent various snapshot CN integration snapshot architectures. Therefore, this work lays the foundation for the feasibility of the proposed FDE under different CN architectures. The applications can also be extended from UAV to other vehicles in different scenarios.

Although the pseudorange observations are simulated in a more realistic scenario by the Spirent simulator, the relative measurements are directly simulated by Gaussian white noise and the

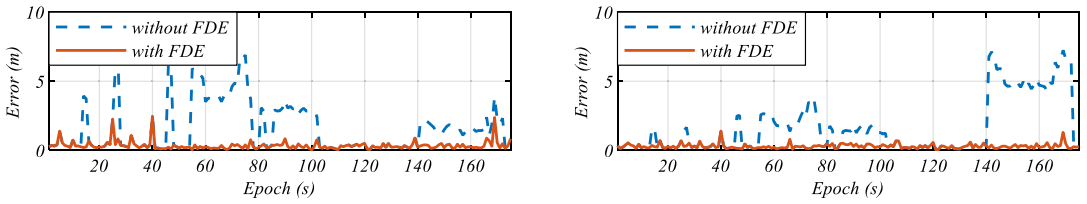

(a) UAV at 400m (b) UAV at 200m

Fig. 23. The comparison between the positioning errors with and without FDE (multipath).

blockage by the buildings is not considered in this work. Besides, the noise models and the multipath effect need to be further analyzed. Therefore, our future work will focus on involving more scenarios in our simulations.

Declaration of competing interest

The authors declare that they have no known competing financial interests or personal relationships that could have appeared to influence the work reported in this paper.

Acknowledgement

This work is supported by the National Natural Science Foundation of China (Grant Number: 62173227 and 62103274) and Laboratory of Science and Technology on Marine Navigation and Control, China State Shipbuilding Corporation (Grant Number: 2021010108). The authors would like to thank Qianxun Spatial Intelligence Inc. for providing the SimGEN-based GSS7000 GNSS simulation system and the Spirent Sim3D software.

References

[1] S. Chung, A. Paranjape, P. Dames, S. Shen, V. Kumar, A survey on aerial swarm robotics, IEEE Trans. Robot. 34 (2018) 837–855.
[2] G. Vachtsevanos, K. Valavanis, Handbook of Unmanned Aerial Vehicles, Springer, 2015.
[3] R. Shakeri, M.A. Al-Garadi, A. Badawy, A. Mohamed, T. Khattab, A.K. Al-Ali, K.A. Harras, M. Guizani, Design challenges of multi-UAV systems in cyber-physical applications: a comprehensive survey and future directions, IEEE Commun. Surv. Tutor. 21 (2019) 3340–3385.
[4] H. Shakhatreh, A. Sawalmeh, A. Al-Fuqaha, Z. Dou, E. Almaita, I. Khalil, N. Othman, A. Khreishah, M. Guizani, Unmanned aerial vehicles (UAVs): a survey on civil applications and key research challenges, IEEE Access 7 (2019) 48572–48634.
[5] A.R. Vetrella, G. Fasano, D. Accardo, Attitude estimation for cooperating UAVs based on tight integration of GNSS and vision measurements, Aerosp. Sci. Technol. 84 (2019) 966–979.
[6] H. Ko, B. Kim, S.H. Kong, GNSS multipath-resistant cooperative navigation in urban vehicular networks, IEEE Trans. Veh. Technol. 64 (2015) 5450–5463.
[7] X. Su, X. Zhan, M. Niu, Y. Zhang, Receiver autonomous integrity monitoring (RAIM) performances of combined GPS/BeiDou/QZSS in urban canyon, IEEJ Trans. Electr. Electron. Eng. 9 (2014) 275–281.
[8] Y. Yuan, F. Shen, X. Li, GPS multipath and NLOS mitigation for relative positioning in urban environments, Aerosp. Sci. Technol. 107 (2020) 106315.
[9] G. Ferri, A. Munafo, A. Tesei, P. Braca, F. Meyer, K. Pelekanakis, R. Petroccia, J. Alves, C. Strode, K. Lepage, Cooperative robotic networks for underwater surveillance: an overview, IET Radar Sonar Navig. 11 (2017) 1740–1761.
[10] F. Ducatelle, G. Di Caro, A. Förster, M. Bonani, M. Dorigo, S. Magnenat, F. Mondada, R. O'Grady, C. Pinciroli, P. Retornaz, V. Trianni, L.M. Gambardella, Cooperative navigation in robotic swarms, Swarm Intell. 8 (2014) 1–33.
[11] C. Zhuang, H. Zhao, S. Hu, C. Sun, W. Feng, Integrity monitoring algorithm for GNSS-based cooperative positioning applications, in: 32nd Int. Tech. Meet. Satell. Div. Inst. Navig. (ION GNSS+ 2019), 2019, pp. 2008–2022.
[12] F. Causa, R. Opromolla, G. Fasano, Cooperative navigation and visual tracking with passive ranging for UAV flight in GNSS-challenging environments, in: 2021 Int. Conf. Unmanned Aircr. Syst., 2021, pp. 1538–1547.
[13] J. Shen, S. Wang, Y. Zhai, X. Zhan, Cooperative relative navigation for multi-UAV systems by exploiting GNSS and peer-to-peer ranging measurements, IET Radar Sonar Navig. 15 (2021) 21–36.
[14] F. Castanedo, A review of data fusion techniques, Sci. World J. 2013 (2013) 704504.
[15] X. Wang, A.K. Gostar, T. Rathnayake, B. Xu, A. Bab-Hadiashar, R. Hoseinnezhad, Centralized multiple-view sensor fusion using labeled multi-Bernoulli filters, Signal Process. 150 (2018) 75–84.
[16] X. Liu, S. Xu, Multi-UAV cooperative navigation algorithm based on federated filtering structure, in: 2018 IEEE CSAA Guid. Navig. Control Conf., IEEE, 2018, pp. 1–5.
[17] S. Tomic, M. Beko, R. Dinis, Distributed RSS-based localization in wireless sensor networks based on second-order cone programming, Sensors (Switz.) 14 (2014) 18410–18432.
[18] F. Shen, J.W. Cheong, A.G. Dempster, A DSRC Doppler/IMU/GNSS tightly-coupled cooperative positioning method for relative positioning in VANETs, J. Navig. 70 (2017) 120–136.
[19] M. Chen, Z. Xiong, J. Liu, R. Wang, J. Xiong, Cooperative navigation of unmanned aerial vehicle swarm based on cooperative dilution of precision, Int. J. Adv. Robot. Syst. 17 (2020) 1–10.
[20] G.M. Hoang, Cooperative Multisensor Localization for Connected Vehicles, Paris Institute of Technology, 2018.
[21] A. Bentaleb, A. Boubetra, S. Harous, Survey of clustering schemes in mobile ad hoc networks, Commun. Netw. 05 (2013) 8–14.
[22] O. Younis, S. Fahmy, HEED: a hybrid, energy-efficient, distributed clustering approach for ad hoc sensor networks, IEEE Trans. Mob. Comput. 3 (2004) 366–379.
[23] P.-H. Tseng, Cluster-based networks for cooperative localisation, IET Radar Sonar Navig. 11 (2017) 605–615.
[24] S. Zhang, H. Zhang, A review of wireless sensor networks and its applications, IEEE Int. Conf. Autom. Logist. (2012) 386–389.
[25] S. Hewitson, J. Wang, GNSS receiver autonomous integrity monitoring (RAIM) performance analysis, GPS Solut. 10 (2006) 155–170.
[26] J. Blanch, T. Walker, P. Enge, Y. Lee, B. Pervan, M. Rippl, A. Spletter, V. Kropp, Baseline advanced RAIM user algorithm and possible improvements, IEEE Trans. Aerosp. Electron. Syst. 51 (2015) 713–732.
[27] J. Xiong, J.W. Cheong, Z. Xiong, A.G. Dempster, S. Member, S. Tian, R. Wang, Integrity for multi-sensor cooperative positioning, IEEE Trans. Intell. Transp. Syst. 22 (2020) 792–807.
[28] M. Wang, H. Qin, T. Jin, Massive terminal positioning system with snapshot positioning technique, GPS Solut. 23 (2019) 1–14.
[29] J.A. Garcia-Molina, J. Fernandez-Rubio, Collaborative snapshot positioning via distributed array processing, in: Proc. 32nd Int. Tech. Meet. Satell. Div. Inst. Navig. (ION GNSS+ 2019), 2019, pp. 1944–1950.
[30] E.D. Kaplan, C.J. Hegarty, Understanding GPS/GNSS: Principles and Applications, third edition, Artech House, 2017.
[31] S. Wang, X. Zhan, Y. Zhai, C. Chi, J. Shen, Highly reliable relative navigation for multi-UAV formation flight in urban environments, Chin. J. Aeronaut. 34 (2021) 257–270.
[32] S. Wang, X. Zhan, Y. Zhai, J. Shen, H. Wang, Performance estimation for Kalman filter based multi-agent cooperative navigation by employing graph theory, Aerosp. Sci. Technol. 112 (2021) 106628.
[33] S. Li, N. Mikhaylov, F. Schiegg, Y. Liu, Performance analysis of collaborative positioning method in automated car driving, in: CEUR Workshop Proc., Tampere, 2020.
[34] Spirent, Spirent Sim3D Datasheet, Datasheet MS3105 Issue 2-00, 2019.
[35] P.K. Enge, The global positioning system: signals, measurements, and performance, Int. J. Wirel. Inf. Netw. 1 (1994) 83–105.
[36] B. Pervan, F.C. Chan, D. Gebre-Egziabher, S. Pullen, P. Enge, G. Colby, Performance analysis of carrier-phase DGPS navigation for shipboard landing of aircraft, Navigation 50 (2003) 181–191.